ARTICLE

Achieving High-Quality Single-Atom Nitrogen Doping of Graphene/SiC(0001) by Ion Implantation and Subsequent Thermal Stabilization

Mykola Telychko,[†,‡] Pingo Mutombo,[†] Martin Ondráček,[†] Prokop Hapala,[†] François C. Bocquet,[§,∞] Jindřich Kolorenč,[⊥] Martin Vondráček,[⊥] Pavel Jelínek,[†,‖] and Martin Švec[†,*]

[†]Institute of Physics, Academy of Sciences of the Czech Republic, Cukrovarnická 10, CZ-16200 Prague, Czech Republic, [‡]Faculty of Mathematics and Physics, Charles University, V Holešovičkách 2, Praha 8, Czech Republic, [§]Peter Grünberg Institut (PGI-3), Forschungszentrum Jülich, 52425 Jülich, Germany, [⊥]Institute of Physics, Academy of Sciences of the Czech Republic, Na Slovance 2, CZ-18221 Prague, Czech Republic, [‖]Graduate School of Engineering, Osaka University, 2-1 Yamada-Oka, Suita, Osaka 565-0871, Japan, and [∞]Jülich-Aachen Research Alliance (JARA)—Fundamentals of Future Information Technology, 52425 Jülich, Germany

ABSTRACT We report a straightforward method to produce high-quality nitrogen-doped graphene on SiC(0001) using direct nitrogen ion implantation and subsequent stabilization at temperatures above 1300 K. We demonstrate that double defects, which comprise two nitrogen defects in a second-nearest-neighbor (meta) configuration, can be formed in a controlled way by adjusting the duration of bombardment. Two types of atomic contrast of single N defects are identified in scanning tunneling microscopy. We attribute the origin of these two contrasts to different tip structures by means of STM simulations. The characteristic dip observed over N defects is explained in terms of the destructive quantum interference.

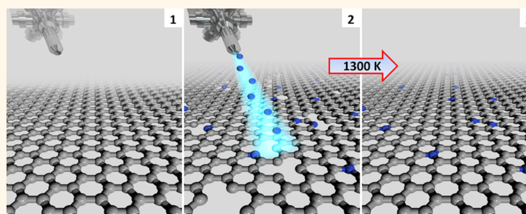

KEYWORDS: graphene · SiC · doping · nitrogen · implantation · STM · photoemission

Graphene has been extensively studied for its outstanding properties.[1−4] However, the electronic structure of the pristine graphene is not suitable for applications in nanoelectronics. Therefore, graphene functionalization, in particular, substitutional doping, has received increased attention lately. Doping, in general, is probably one of the most explored routes of tuning the electronic properties of pristine graphene. The substitution of carbon atoms by nitrogen gives rise to donor states inducing n-type conductivity.[5]

One approach to produce N-doped graphene is a direct growth of modified layers by chemical vapor deposition (CVD)[6−9] or a simple addition of N during the growth in a molecular form or as a pure gas.[10−12] Stability of such defects over time and their response to ambient conditions is not well understood yet. The chemistry-based methods, despite their success and potential for mass production, usually suffer from undesired contamination and incorporation of different types of N substitutions, pyridine-like or pyrrole-like.[13]

Alternatively, N doping of C-based materials *via* low-energy ion implantation has been proposed. Ion implantation is the standard technique used for integrated circuit fabrication in the semiconductor industry. Joucken *et al.*[14] exposed epitaxial graphene grown on SiC(0001) to an atomic nitrogen ion flux produced by an *in situ* radio frequency plasma source. By means of scanning tunneling microscopy (STM), they observed the N substitutional defects and also other unknown structures associated with the disruptive action of the ion beam. Very recently, Bangert *et al.*[15] reported ion implantation of N into free-standing graphene. They found about 90% of nitrogen atoms in the single substitutional configuration. In these methods, a multitude of defect types can also be created. Despite the advances, there is still a shortage of methods that provide high-quality doping of graphene with N atoms exclusively located at substitutional

* Address correspondence to svec@fzu.cz.

Received for review April 30, 2014 and accepted June 2, 2014.

Published online June 02, 2014
10.1021/nn502438k

© 2014 American Chemical Society

positions and without any undesired impurities or derivatives.

In this work, we propose a modified preparation scheme to produce high-quality N-doped graphene using direct N ion implantation and subsequent stabilization at temperatures above 1300 K in ultrahigh vacuum (UHV) conditions. Using this method, the doped graphene/SiC(0001) is prepared with the exclusive presence of N atoms in the substitutional positions. If the procedure is repeated or the duration of ion bombardment is extended, besides the single N defects, we also observe formation of double defects, which are located in the second-nearest-neighbor position (meta configuration). Both observed N defects remain stable even under exposure to ambient conditions. Scanning tunneling microscopy and density functional theory (DFT) calculations were used for a detailed characterization of the electronic structure of these defects. Two main types of atomic contrast of the defects were observed. We rationalize the observed atomic contrast by means of DFT calculations and show, for the first time, that the quantum interference governs the electron transport between the STM tip and the N defect.

Figure 1a shows a typical high-resolution STM image of the N-doped bilayer graphene (BLG) on 6H-SiC(0001) after 10 min of 100 eV ion bombardment using N gas and subsequent annealing to 1300 K for 10 min. The graphene layer is decorated by randomly distributed characteristic triangle-shaped objects that are present in two basic orientations with respect to the graphene lattice. The two orientations of the triangles are produced by the locations of the substitutional N atoms in one of the two graphene sublattices. The defect concentration is ultralow: <0.04% of all C atoms in the graphene layer are substituted with N defects. The number of defects that are distinct from the single substitutional atoms is negligible in the STM images. We should note that identical defects were also found on the single-layer graphene, with a reduced quality of detail due to a higher apparent corrugation of single-layer graphene.

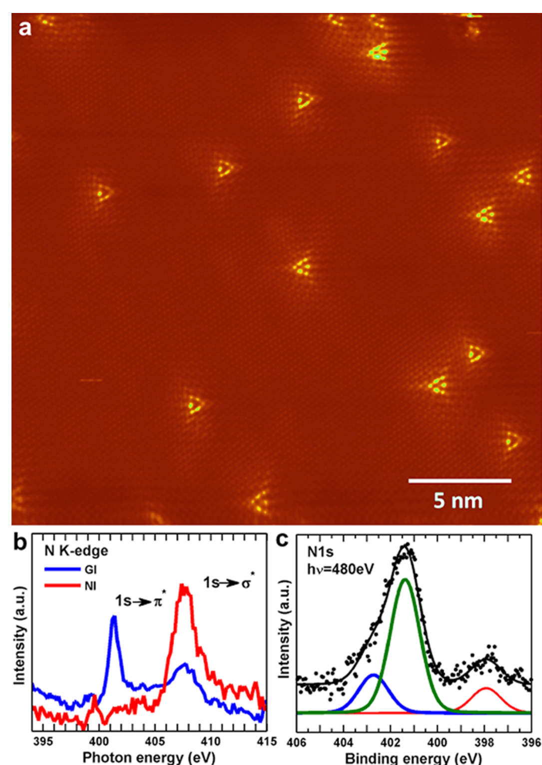

Figure 1. (a) Constant-height STM image of the N-doped BLG on 6H-SiC(0001) after 10 min of 100 eV ion bombardment using N gas and subsequent annealing to 1300 K. The tunneling bias was set to −0.3 V. (b) Absorption spectra near the N K-edge showing the π^* and σ^* resonances of the N incorporated in the graphene honeycomb lattice and (c) photoemission peak of N 1s fitted with three components.

To get more insight into binding character of N defects in graphene, we performed near-edge X-ray absorption fine structure spectroscopy and measured a highly resolved spectrum of the N 1s photoemission line. The K-edge absorption spectra in Figure 1b corroborate that the ion-implanted N atoms are a part of the graphene π system, manifesting clear π^* and σ^* resonances in the normal and grazing incidence, similarly to the C K-edge absorption in graphene (not shown). The dominant components of the photoemission N 1s structure in Figure 1c are located near 401.5 and 403 eV (binding energy). These are most likely associated with the majority of the N substitutional defects on the single-layer (403 eV) and bilayer (401.5 eV) graphene, as seen in the STM images. The smallest component at 398 eV accounts for 11% of the total N 1s intensity, and it is usually associated with the pyridine-like N atoms;[10,12] however, in our STM images, we do not observe any objects that could be linked to such type of defects. Therefore, this component could be assigned either to N defects in the buffer layer fraction on the substrate or to some type of N atom configuration in the subgraphene area (*e.g.*, the Si−N bond).[16]

Multiple sessions of atomically resolved current imaging in the constant-height mode demonstrated that the STM contrast on the N defects usually results in one of two characteristic patterns. Figure 2 shows an equal-scale comparison of these two most frequently observed contrast types. Since the graphene lattice is very discernible in the vicinity of the defects, it is possible to overlay the honeycomb graphene lattice over both current maps of the two contrast types (insets of Figure 2a,b). It helps to identify the atomic structure and assign the lattice positions to the tunneling current maxima around the defects. Figure 2a shows N defects that appear as hollow triangles, each composed of six protrusions, which correspond to the six carbon atoms located around the defect. This type of contrast is very similar to the one observed previously.[14] On the other hand, Figure 2b shows an equivalent type of N defects imaged as triangles

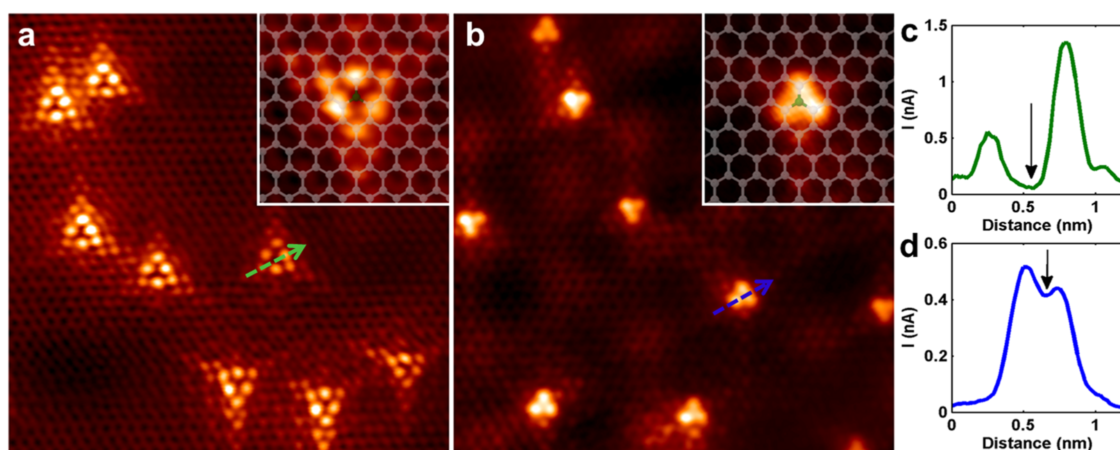

Figure 2. Pair of 9 × 9 nm^2 current maps (constant height) of graphene with substitutional N defects exhibiting the two most frequently observed atomically resolved contrasts: (a) hollow triangle contrast and (b) full triangle contrast, bias −0.4 V. The insets show the registry of the defects with respect to the graphene lattice. (c,d) Line profiles of the tunneling current corresponding to the lines indicated in (a) and (b), respectively. The arrows mark the positions of the tunneling current minima at the centers of the defect images.

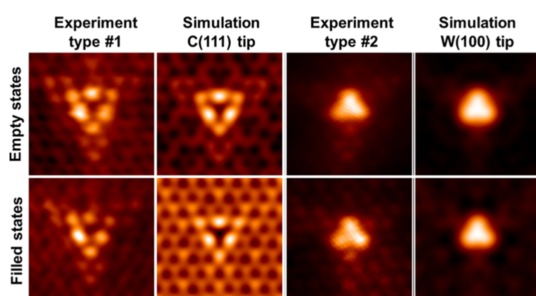

Figure 3. Experimental and calculated STM current maps of the single N defects, empty and filled states, 1.7 × 1.7 nm^2. STM simulations (+0.5 and −0.5 V, surface−tip distance 3.5 Å) for various tip models are matched to the two most frequently experimentally observed patterns (+0.4 and −0.4 V).

composed of only three protrusions packed closely together, which coincide with the three nearest-neighbor carbon atoms around the defect.

In order to rationalize the origin of these two types of atomic contrast, we performed STM simulations based on DFT total energy calculations with different tip models (for details, see Methods). For a carbon tip, C(111), an apex with the diamond structure was used; for a tungsten W(100) tip, the structure was derived from a body-centered cubic structure. For these two tips, we found a very good agreement between the experimental and theoretical current images in both the empty and filled states (see Figure 3). In particular, the image simulated with the C(111) tip reproduces closely the features of the hollow triangle contrast. The second type of contrast matches well with the maps simulated with a tip made of W(100).

The applicability of these two tip models can be justified by the experimental circumstances. First, all the defects are imaged with the same contrast type within each image; therefore, it is beyond any doubt that the dual type of atomically resolved contrast is caused by different terminations of the scanning probe apex. Second, since the W tip was annealed before every measurement by a W filament and treated by voltage and *z*-pulses during the experimental session, it is very likely that the composition of the STM probe apex varies from the pure W to pure C.

In addition, we performed site-dependent measurements of the differential conductance d*I*/d*V* (Figure 4a) to analyze the effect of the N atoms on the electronic structure of graphene. Our d*I*/d*V* spectra are similar to previously published data.[9,14] On the N atom, we observed two characteristic depressions: at zero bias and near −400 mV (green arrow in Figure 4a). The latter is associated with the Dirac point, which is shifted toward lower energies with respect to undoped graphene on the same substrate (near −350 mV, marked by the blue arrow) due to the presence of N defects. The dip at zero bias has been explained in terms of inelastic tunneling accompanied by excitation of an optical phonon mode in pristine graphene monolayers that enhances the tunneling current outside the gap.[17]

We would like to note that in both types of STM contrast and in the d*I*/d*V* spectroscopy, the tunneling current detected over N defects is weaker than that over the nearest carbon atoms (see the STM line profiles in Figure 2c,d). This appears to be in a striking contradiction with the results of our DFT calculations, which show a negligible vertical relaxation of the N atom out of the graphene plane and, more importantly, a pronounced peak in the density of states near the Fermi level (see Figure 4b). Thus, assuming that the tunneling current is simply proportional to the local electron density on the sample, we should observe an increased tunneling current above N atoms with respect to the surrounding C atoms, which is not the case. In the following, we will show that for the N defects such assumption is not valid, and that the

decrease in the tunneling current is a consequence of a destructive quantum interference.

First, let us analyze the character of the interaction between the π-orbitals of N and the nearest-neighbor C atoms. Near the Fermi level, they form an electronic state which has a node located between these two atoms. Consequently, the corresponding off-diagonal element of the density matrix has a negative value. On the contrary, the density matrix element of the C−C bond π-orbitals has a positive value. The negative value of the off-diagonal element of the C−N π-bonds gives rise to a destructive interference among different tunneling channels between the tip and either the N atom or the nearest C atoms.

To demonstrate this phenomenon directly, we calculated the tunneling current for the C(111) tip above the N defect, selectively allowing the tunneling process through (i) all surface atoms (I_{tot}^N), (ii) only the N atom (I_N^N), or (iii) only the three neighboring C atoms (I_C^N); see Figure 4c. The $I_{tot}^N(z)$ curve shows a pronounced dip at close tip−sample distances when compared to the individual I_C^N and I_N^N current channels. The tunneling current is proportional to the square of a corresponding quantum-mechanical amplitude. Assuming ideally destructive interference, we can approximate the amplitude for the resulting tunneling current I_{sim}^N by a difference between amplitudes for the partial flows through the N atom and through the C atoms: $I_{sim}^N = (\sqrt{I_C^N} - \sqrt{I_N^N})^2$. From Figure 4c, it is evident that the tunneling current I_{sim}^N calculated using this formula has a remarkably similar character to I_{tot}^N. In addition, I_{tot}^N is smaller than I_{tot}^C, the total tunneling current calculated for the tip placed above one of the C neighbors, in the whole range of tip−sample distances. Therefore, we attribute the depression of the tunneling current near the N defect to the destructive interference of the electron wave functions originating from the C and N atoms.

The implantation of the N atoms into the graphene lattice can be continued progressively. Figure 5 shows the same surface as shown in Figure 1a, but with a higher amount of defects. These were produced by a

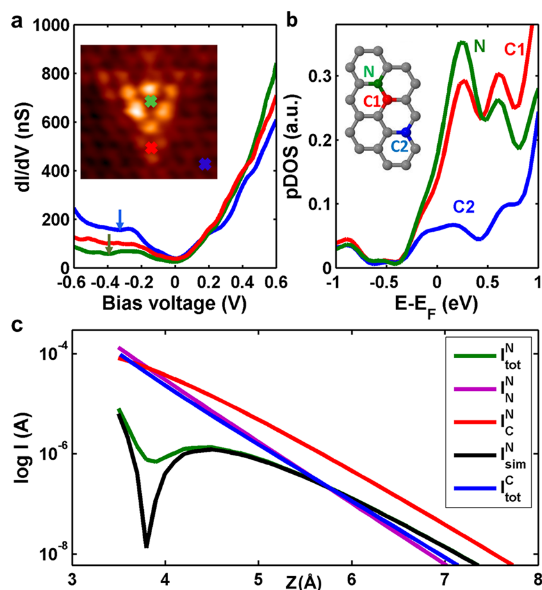

Figure 4. (a) Experimental d*I*/d*V* spectroscopy taken at different positions: (i) above N defect (green); (ii) in the surrounding of the defect (red); and (iii) on the graphene region (blue). The spectra were taken at I_{set} = 1.0 nA. The arrows mark the dips in the spectra for the N atom and the surrounding graphene. (b) Plots of the calculated projected density of states for N defect and two different C atoms as indicated in the inset. (c) Calculated tunneling current on the N defect as a function of distance for N and C channels separately (I_N^N and I_C^N, respectively), the calculated total current (I_{tot}^N) including all channels, and a model using the formula $I_{sim} = (\sqrt{I_C^N} - \sqrt{I_N^N})^2$. The dip in I_{tot}^N marks the presence of a destructive interference in the electron tunneling. For comparison with the I_{tot}^N on the N defect, the total tunneling current for the tip placed on one of the nearest-neighbor C atoms (I_{tot}^C) is also shown. The upper index denotes position of the tip above N or the nearest-neighbor C atom.

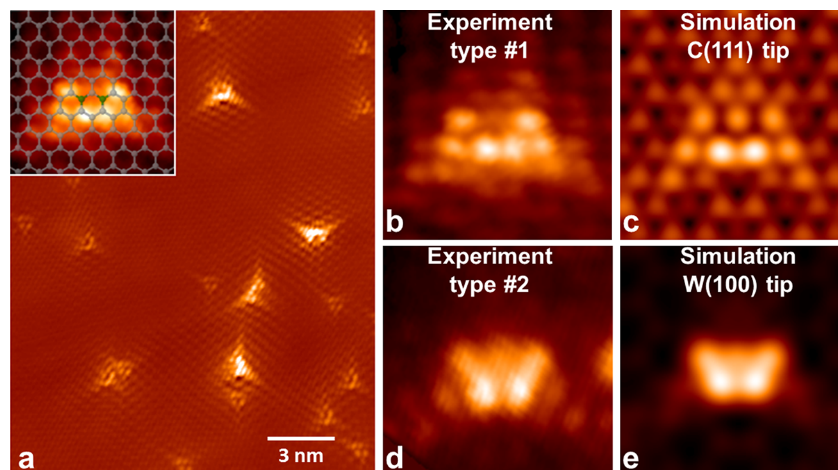

Figure 5. (a) STM image of a sample doped with a higher amount of N defects; the inset shows an overlay of the graphene lattice with two substitutional N defects on a zoomed meta defect. (b−e) Experiment to theory comparison of the two types of the most frequently observed atomically resolved contrasts.

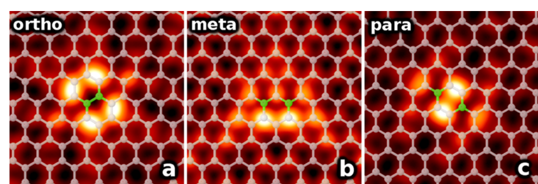

Figure 6. Calculated filled states, constant-height STM images, and a ball-and-stick model overlays of the three basic two-atom N defects, obtained at −0.5 V, with 3.5 Å tip−sample separation. The configurations are (a) ortho, (b) meta, and (c) para.

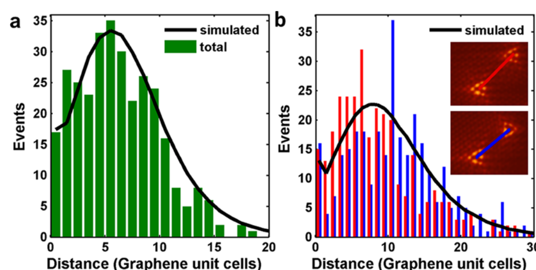

Figure 7. Histograms of the experimental nearest-neighbor distances for (a) all defects independently of the sublattice and (b) depending on the sublattice, showing a preference for shorter distances for the defects that reside in the same sublattice. The simulated histograms of the nearest-neighbor distances are evaluated on a random spatial distribution of defects without any preference.

repeated ion irradiation and high-temperature annealing of the substrate. The concentration of the N defects is ≈0.13%, and a new type of structure emerges. This new structure has only one axis of mirror symmetry, unlike the single N defect, which has three. Moreover, it is present in six different orientations. An overlay of the graphene lattice (the inset of Figure 5a) suggests a possible atomic structure consisting of a couple of substitutional N atoms in the second-nearest-neighbor configuration (meta). To support this interpretation, we simulated the current maps using the identical method as in the case of the single N defects with the two tips and compared the results to the experimental current maps in both major types of contrast. The agreement is very good, as it can be seen in Figure 5b−e. The substantial differences among the most simple two-atom N defects can be appreciated in Figure 6, where all the three ortho, meta, and para configurations are overlaid onto the corresponding filled states' STM simulation with the C(111) tip.

We discuss statistical analysis of N defects based on STM images from the total inspected area of >3100 nm^2. The meta defects represent ≈10% of the total amount of defects. On the other hand, only a very limited amount of double defects is detected that could be candidates for the first-neighbor (ortho) or third-nearest-neighbor (para) configurations of N atoms in the graphene lattice (<2% of all observed double defects). A feasible explanation of such prevalence of the meta configuration could be that it is substantially energetically favored in comparison to the other arrangements of the double defect. To test the conjecture, we evaluated the total energies of the ortho, meta, and para configurations (see Figure 6) in the free-standing graphene using the DFT methods. Surprisingly, the most stable arrangement was the para, having its total energy 0.3 eV lower than the meta configuration, in agreement with the previous study.[18] This energy difference is largely independent of the exchange-correlation functional used in the calculation. Similarly to the single substitutional defects, the theory does not indicate any substantial relaxation of the N atoms out of the graphene plane.

Since systems with lowered dimensionality are known to be difficult for DFT, we computed the total energies of the meta and para double defects also with a more accurate electronic structure method, namely, the fixed-node/fixed-phase quantum Monte Carlo (QMC) method[19] that employs explicitly correlated many-body wave functions. Our QMC calculations indicate that the para configuration is more stable than the meta by 0.53 ± 0.09 eV, where the quoted error is due to the stochastic nature of the QMC method. We believe that the discrepancy between the thermodynamic arguments and the observed relative abundance of the double defects is a hint that kinetic factors may play an important role during the formation of these defects. Nevertheless, it remains an open question and a full understanding of this phenomenon requires further research.

A histogram of the nearest distances between the N defects (treating the double defects as separate single defects) is consistent with a simulated random distribution at the same defect concentration (Figure 7a). The experimental mean nearest distance between all the N defects without distinguishing the sublattices is 2.59 nm. The simulation gives 2.53 nm, in a very good agreement with the experimental value. However, if the histograms are evaluated separately for the nearest distances of the defects in the same sublattices or in the opposite sublattice (Figure 7b), there is a significant split of the mean values for these cases. The mean nearest distance for the defects in the same sublattice is 3.63 nm, whereas the mean nearest distance for the defects that are in the opposite sublattices is significantly larger: 3.99 nm. Both histograms notably differ from the simulation of a random distribution, which has a mean value of 3.69 nm. This can be interpreted as a preference to form the defects on the same sublattice near each other. Such preference has also been reported for the case of doping by CVD methods;[9] some CVD procedures even resulted in much stronger sublattice preference than our implantation method.[20] Similar trend has been found recently also on Mo implanted in graphene.[21]

In our further attempts to increase the concentration by repeating the ion implantation procedure, we have finally reached a saturation. The maximum

concentration of the N defects observed on the bilayer graphene reached ≈1.6%. All the surfaces prepared using this method are remarkably stable. Even after exposure to the ambient conditions, the modified graphene layer did not change its physical properties; after reinsertion into the UHV and degassing at 1100 K, the sample exhibited the same picture as before.

In conclusion, we devised a robust method for preparation of N-doped graphene in UHV conditions, with exclusive presence of the N defects in the substitutional positions. At higher concentrations of the N atoms in the graphene lattice, we observe the formation of double defects located in the second-nearest-neighbor (meta) position. The doping can be scaled up to a concentration 1.6% and remains fully stable even under exposure to ambient conditions. We rationalized the atomically resolved STM images of the single and meta N defects by different tip models. A destructive quantum interference effect explains the characteristic dip over N defetcs observed in STM images.

METHODS

The experiments were performed in ultrahigh vacuum, variable-temperature STM, with base pressure below 5×10^{-10} mbar. Sample was a $4.0 \times 10.0 \times 0.5$ mm^3 stripe of n-type Si-terminated 6H-SiC(0001) cut from a wafer (Semiconductor Wafer, Inc.) using a diamond tip. The sample was handled with nonmetallic tweezers to prevent metal contamination,[22] mounted on a molybdenum sample holder, and inserted into the chamber. The preparation procedure included Si evaporation and repeated annealing of the sample, as described in detail by other authors.[23−25] At the end, the composition of the surface was dominated by bilayer graphene; however, single-layer graphene and trilayer graphene regions were also present. Defects in graphene lattice were created by bombarding with 100 eV ions created using a standard electron-impact ion gun and a N_2 gas (99.999% purity). N_2 back pressure during this process was kept at 5×10^{-7} mbar; the acceleration energy of the electrons inside the ion gun was 100 eV. In the next step, the surface was healed and stabilized by annealing the sample up to 1300 K. In the current experiments, the defect concentration was roughly proportional to the exposure time. W tips were used for the measurements, and both the sample and the tip apex were annealed to 1300 K for 5 min before each new measurement session. The photoemission was performed at Elettra synchrotron lightsource at the Materials Science Beamline. The N K-edge absorption spectrum yield was integrated at the valence band (from a binding energy of 60 eV to the Fermi level).

We used 7×7 supercell of a free-standing single-layer graphene to simulate the N doping with the DFT method. The supercell contained one N atom or two N atoms in ortho, meta, or para configurations. The equilibrium positions of atoms were found using Vienna Ab Initio Simulation Package (VASP),[26] a plane wave *ab initio* code. Vanderbilt ultrasoft pseudopotentials[27] for C and N were used. The plane wave cutoff was set to 348 eV. The exchange-correlation functional was approximated with the PW91 variant of the generalized gradient approximation (GGA).[28] The Brillouin zone corresponding to the supercell was sampled with 6×6 *k*-points. The calculations were not spin-polarized. Two carbon atoms, chosen as the most distant ones from the N atom(s), were kept fixed during the relaxation. The criterion for equilibrium was that forces on all except the two fixed atoms had to be smaller than 0.001 eV/Å.

The optimized geometries were then used in STM simulations,[29] with tight-binding Hamiltonian obtained by local-orbital DFT code Fireball[30] using an optimized pseudoatomic orbital basis set.[31] An sp basis set was used for both C and N atoms. Several preoptimized realistic tip models were picked for the simulation: a Si(111) tip, a (111)-oriented carbon tip with diamond-like structure, a W(100) tip, and a more simplified model consisting of just one d-orbital of tungsten. The STM images were simulated in the constant-height mode.

The QMC simulations are substantially more computationally demanding than DFT, and hence only a smaller 4×4 supercell of graphene was used in the QMC study of the double defects. Only the ideal planar geometry was considered since the DFT calculations did not show any substantial relaxation of the lattice structure around the N substitutions. We employed the diffusion Monte Carlo method as implemented in the QWalk code,[32] with the phase of the many-body wave function fixed by a Slater−Jastrow trial function. The Slater part of the wave function ansatz was built out of GGA single-particle orbitals obtained with the Gaussian DFT program Crystal.[33] The core electrons were represented by norm-conserving pseudopotentials,[34] and a corresponding spd basis was used for the valence electrons. The finite-size effects induced by incorrect momentum quantization due to the confinement of electrons into the finite supercell were reduced by averaging over the so-called twisted boundary conditions,[19,35] which corresponded to a sampling of the supercell Brillouin zone by an 8×8 *k*-point mesh. The finite-size errors due to the approximation to the long-range tail of the Coulomb potential were not explicitly addressed; nevertheless, these errors mostly cancel out in the differences of the total energies that are of interest here.

Conflict of Interest: The authors declare no competing financial interest.

Acknowledgment. This work was supported by the Czech Science Foundation (GAČR) through Project No. 14-02079S. The Materials Science Beamline and M.V. are supported by the Ministry of Education of the Czech Republic under grants LG12003 and LM2011029. F.C.B. acknowledges the financial support from the Initiative and Networking Fund of the Helmholtz Association, Postdoc Programme VH-PD-025.

REFERENCES AND NOTES

1. Castro Neto, A. H.; Guinea, F.; Peres, N. M. R.; Novoselov, K. S.; Geim, A. K. The Electronic Properties of Graphene. *Rev. Mod. Phys.* **2009**, *81*, 109–162.
2. Geim, A. K.; Novoselov, K. S. The Rise of Graphene. *Nat. Mater.* **2007**, *6*, 183–191.
3. Geim, A. K. Graphene: Status and Prospects. *Science* **2009**, *324*, 1530–1534.
4. Novoselov, K. S.; Geim, A. K.; Morozov, S. V.; Jiang, D.; Zhang, Y.; Dubonos, S. V.; Grigorieva, I. V.; Firsov, A. A. Electric Field Effect in Atomically Thin Carbon Films. *Science* **2004**, *306*, 666–669.
5. Schiros, T.; Nordlund, D.; Palova, L.; Prezzi, D.; Zhao, L.; Kim, K. S.; Wurstbauer, U.; Gutierrez, C.; Delongchamp, D.; Jaye, C.; *et al.* Connecting Dopant Bond Type with Electronic Structure in N-Doped Graphene. *Nano Lett.* **2012**, *12*, 4025–4031.
6. Meyer, J. C.; Kurasch, S.; Park, H. J.; Skakalova, V.; Künzel, D.; Grob, A.; Chuvilin, A.; Algara-Siller, G.; Roth, S.; Iwasaki, T.; *et al.* Experimental Analysis of Charge Redistribution Due to Chemical Bonding by High-Resolution Transmission Electron Microscopy. *Nat. Mater.* **2011**, *10*, 210.
7. Lu, Y.-F.; Lo, S.-T.; Lin, J.-C.; Zhang, W.; Lu, J.-Y.; Liu, F.-H.; Tseng, C.-M.; Lee, Y.-H.; Liang, C.-T.; Li, L.-J. Nitrogen-Doped Graphene Sheets Grown by Chemical Vapor Deposition: Synthesis and Influence of Nitrogen Impurities on Carrier Transport. *ACS Nano* **2013**, *7*, 6522–6532.

8. Wei, D.; Liu, Y.; Wang, Y.; Zhang, H.; Huang, L.; Yu, G. Synthesis of N-Doped Graphene by Chemical Vapor Deposition and Its Electrical Properties. *Nano Lett.* **2009**, *9*, 1752–1758.
9. Zhao, L.; He, R.; Rim, K. T.; Schiros, T.; Kim, K. S.; Zhou, H.; Gutierrez, C.; Chockalingam, S. P.; Arguello, C. J.; Palova, L.; *et al.* Visualizing Individual Nitrogen Dopants in Monolayer Graphene. *Science* **2011**, *333*, 999–1003.
10. Zhao, W.; Höfert, O.; Gotterbarm, K.; Zhu, J.; Papp, C.; Steinrück, H.-P. Production of Nitrogen-Doped Graphene by Low-Energy Nitrogen Implantation. *J. Phys. Chem. C* **2012**, *116*, 5062–5066.
11. Wang, H.; Xie, M.; Thia, L.; Fisher, A.; Wang, X. Strategies on the Design of Nitrogen-Doped Graphene. *J. Phys. Chem. Lett.* **2014**, *5*, 119–125.
12. Velez-Fort, E.; Mathieu, C.; Pallecchi, E.; Pigneur, M.; Silly, M. G.; Belkhou, R.; Marangolo, M.; Shukla, A.; Sirotti, F.; Ouerghi, A. Epitaxial Graphene on 4H-SiC(0001) Grown under Nitrogen Flux: Evidence of Low Nitrogen Doping and High Charge Transfer. *ACS Nano* **2012**, *6*, 10893–10900.
13. Soin, N.; Sinha Roy, S.; Roy, S.; Hazra, K. S.; Misra, D. S.; Lim, T. H.; Hetherington, C. J.; McLaughlin, J. A. Enhanced and Stable Field Emission from *In Situ* Nitrogen-Doped Few-Layered Graphene Nanoflakes. *J. Phys. Chem. C* **2011**, *115*, 5366–5372.
14. Joucken, F.; Tison, Y.; Lagoute, J.; Dumont, J.; Cabosart, D.; Zheng, B.; Repain, V.; Chacon, C.; Girard, Y.; Botello-Méndez, A. R.; *et al.* Localized State and Charge Transfer in Nitrogen-Doped Graphene. *Phys. Rev. B* **2012**, *85*, 161408.
15. Bangert, U.; Pierce, W.; Kepaptsoglou, D. M.; Ramasse, Q.; Zan, R.; Gass, M. H.; Van den Berg, J. A.; Boothroyd, C. B.; Amani, J.; Hofsäss, H. Ion Implantation of Graphene—Toward IC Compatible Technologies. *Nano Lett.* **2013**, *13*, 4902–4907.
16. Yamamoto, K.; Koga, Y.; Fujiwara, S. XPS Studies of Amorphous SiCN Thin Films Prepared by Nitrogen Ion-Assisted Pulsed-Laser Deposition of SiC Target. *Diamond Relat. Mater.* **2001**, *10*, 1921–1926.
17. Zhang, Y.; Brar, V. W.; Wang, F.; Girit, C.; Yayon, Y.; Panlasigui, M.; Zettl, A.; Crommie, M. F. Giant Phonon-Induced Conductance in Scanning Tunnelling Spectroscopy of Gate-Tunable Graphene. *Nat. Phys.* **2008**, *4*, 627.
18. Lv, R.; Li, Q.; Botello-Méndez, A. R.; Hayashi, T.; Wang, B.; Berkdemir, A.; Hao, Q.; Elías, A. L.; Cruz-Silva, R.; Gutiérrez, H. R.; *et al.* Nitrogen-Doped Graphene: Beyond Single Substitution and Enhanced Molecular Sensing. *Sci. Rep.* **2012**, *2*, 586.
19. Kolorenč, J.; Mitas, L. Applications of Quantum Monte Carlo Methods in Condensed Systems. *Rep. Prog. Phys.* **2011**, *74*, 026502.
20. Zabet-Khosousi, A.; Zhao, L.; Pálová, L.; Hybertsen, M. S.; Reichman, D. R.; Pasupathy, A. N.; Flynn, G. W. Segregation of Sublattice Domains in Nitrogen-Doped Graphene. *J. Am. Chem. Soc.* **2014**, *136*, 1391–1397.
21. Wan, W.; Li, H.; Huang, H.; Wong, S. L.; Lv, L.; Gao, Y.; Wee, A. T. S. Incorporating Isolated Molybdenum (Mo) Atoms into Bilayer Epitaxial Graphene on 4H-SiC(0001). *ACS Nano* **2014**, *8*, 970–976.
22. Harris, G. *Properties of Silicon Carbide*; EMIS datareviews series; INSPEC, Institution of Electrical Engineers, 1995.
23. Riedl, C.; Coletti, C.; Starke, U. Structural and Electronic Properties of Epitaxial Graphene on SiC(0001): A Review of Growth, Characterization, Transfer Doping and Hydrogen Intercalation. *J. Phys. D: Appl. Phys.* **2010**, *43*, 374009.
24. Huang, H.; Chen, W.; Chen, S.; Wee, A. T. S. Bottom-up Growth of Epitaxial Graphene on 6H-SiC(0001). *ACS Nano* **2008**, *2*, 2513–2518.
25. Hass, J.; de Heer, W. A.; Conrad, E. H. The Growth and Morphology of Epitaxial Multilayer Graphene. *J. Phys.: Condens. Matter* **2008**, *20*, 323202.
26. Kresse, G.; Furthmüller, J. Efficient Iterative Schemes for *Ab Initio* Total-Energy Calculations Using a Plane-Wave Basis Set. *Phys. Rev. B* **1996**, *54*, 11169–11186.
27. Vanderbilt, D. Soft Self-Consistent Pseudopotentials in a Generalized Eigenvalue Formalism. *Phys. Rev. B* **1990**, *41*, 7892–7895.
28. Perdew, J. P.; Chevary, J. A.; Vosko, S. H.; Jackson, K. A.; Pederson, M. R.; Singh, D. J.; Fiolhais, C. Atoms, Molecules, Solids, and Surfaces: Applications of the Generalized Gradient Approximation for Exchange and Correlation. *Phys. Rev. B* **1992**, *46*, 6671–6687.
29. Blanco, J. M.; Flores, F.; Pérez, R. STM-Theory: Image Potential, Chemistry and Surface Relaxation. *Prog. Surf. Sci.* **2006**, *81*, 403–443.
30. Lewis, J.; Jelínek, P.; Ortega, J.; Demkov, A.; Trabada, D.; Haycock, B.; Wang, H.; Adams, G.; Tomfohr, J.; Abad, E.; *et al.* Advances and Applications in the FIREBALL *Ab Initio* Tight-Binding Molecular-Dynamics Formalism. *Phys. Status Solidi B* **2011**, *248*, 1989–2007.
31. Basanta, M.; Dappe, Y.; Jelínek, P.; Ortega, J. Optimized Atomic-like Orbitals for First-Principles Tight-Binding Molecular Dynamics. *Comput. Mater. Sci.* **2007**, *39*, 759–766.
32. Wagner, L. K.; Bajdich, M.; Mitas, L. QWalk: A Quantum Monte Carlo Program for Electronic Structure. *J. Comput. Phys.* **2009**, *228*, 3390–3404.
33. Saunders, V. R.; Dovesi, R.; Roetti, C.; Orlando, R.; Zicovich-Wilson, C. M.; Harrison, N. M.; Doll, K.; Civalleri, B.; Bush, I.; D'Arco, P.; *et al. CRYSTAL2003 User's Manual*; University of Torino: Torino, Italy, 2003.
34. Ovcharenko, I.; Aspuru-Guzik, A.; Lester, W. A. Soft Pseudopotentials for Efficient Quantum Monte Carlo Calculations: From Be to Ne and Al to Ar. *J. Chem. Phys.* **2001**, *114*, 7790–7794.
35. Lin, C.; Zong, F. H.; Ceperley, D. M. Twist-Averaged Boundary Conditions in Continuum Quantum Monte Carlo Algorithms. *Phys. Rev. E* **2001**, *64*, 016702.